Experimental Demonstration of Dark-State Metasurface Laser with Controllable Radiative Coupling

Sotiris Droulias,* Sughra Mohamed, Heikki Rekola, Tommi K. Hakala,* Costas M. Soukoulis, and Thomas Koschny

Lasing at the nanoscale using plasmonic nanoparticles offers the prospect of strong field concentration, hence strong light–matter interactions, low lasing thresholds, and ultrafast operation. However plasmonic nanoparticles suffer from high dissipative and radiative losses, the latter being rigidly tied to the shape of the nanoparticles and symmetry of their localized plasmon resonant modes. To overcome this limitation, recent theoretical work proposes using direct lasing into dark surface states to construct lasers that conceptually allow for independent implementation of the lasing state and its coherent radiation output. Here, lasing in dark resonant states of a metasurface laser and controllable coherent outcoupling of radiation with the aid of a tightly coupled, weakly radiative metasurface are demonstrated experimentally. The laser is implemented using a thin, low-loss dielectric film supporting surface mode-like dark dielectric bound states and the coupling metasurface is composed of small non-resonant scatterers that controllably but weakly perturb the dark mode and turn it partially bright. Distinct far-field signatures that can be observed experimentally for both dark and bright lasing are identified and demonstrated. The scalability of this design, here implemented for lasing in the near-infrared, enables large-aperture ultra-thin coherent light sources with controllable emission from the infrared to the visible.

S. Droulias,[+] C. M. Soukoulis
Institute of Electronic Structure and Laser
FORTH
Heraklion, Crete 71110, Greece
E-mail: sdroulias@iesl.forth.gr
S. Mohamed, H. Rekola, T. K. Hakala
Institute of Photonics
University of Eastern Finland
Joensuu FI-80101, Finland
E-mail: tommi.hakala@uef.fi
C. M. Soukoulis, T. Koschny
Ames Laboratory and Department of Physics and Astronomy
Iowa State University
Ames, IA 50011, USA

ⓘ The ORCID identification number(s) for the author(s) of this article can be found under https://doi.org/10.1002/adom.202102679.

[+]Present address: Department of Digital Systems, University of Piraeus, Piraeus 18534, Greece

1. Introduction

Lasing typically requires a gain medium and a configuration that provides resonant optical feedback.[1] In conventional, macroscopic laser systems this is achieved with propagating waves that bounce back and forth between mirrors, where the enclosed space between the mirrors forms a cavity that contains the gain medium. However, as the laser dimensions are pushed to smaller scales, less space is left for the waves to propagate. Thus, in order to maintain strong interaction of light with the gain medium, alternative feedback schemes become crucial. At the nanoscale, typical nanolasers overcome this limitation by using feedback that relies on resonant near fields of dressed photonic states, rather than free propagating waves. In essence, with high Q modes, the required long interaction distances that propagating waves must travel can be exchanged with long interaction times, therefore achieving significantly reduced laser volume, practically in the order of the spatial extent of the near fields (≈100 nm length scales).

Owing to their strong, sub-wavelength field confinement, surface plasmon-polariton modes have been successfully used for constructing lasers of sub-wavelength size.[2–10] However, the large ohmic losses associated with the metals, which are necessary for the plasmonic response, push the lasing threshold to high levels. Importantly, the radiation damping is closely connected with the type and symmetry of the oscillating plasmonic mode and, hence, it is difficult to control the outcoupled power for a given mode. Also, it is difficult to achieve large coherent emitting apertures necessary for direct beam formation without external optics. To overcome these limitations, in recent years, alternative approaches based on high-index dielectrics have been proposed, usually involving Mie resonances,[11,12] anapole states,[13] bound states in the continuum,[14–17] and topological phases.[18–20] The low absorption of dielectrics allows for high-Q modes to be sustained, however, controllable outcoupling of the lasing power independent of the lasing mode remains still an unresolved challenge. Dark resonant surface modes based on dielectric films, on the other hand, have been theoretically predicted to provide low lasing thresholds and controllable emission[21–23] while lasing in dark and bright modes of finite-sized arrays of

**ADVANCED
SCIENCE NEWS**

www.advancedsciencenews.com

**ADVANCED
OPTICAL
MATERIALS**

www.advopticalmat.de

plasmonic nanoparticles has been demonstrated experimentally.[24] The key element enabling this control over the radiative emission is that these dark lasing states are modes of zero net electric or magnetic moment that, consequently, do not radiate. They simply implement resonant photonic states that serve as resonant energy storing elements, similar to conventional cavities of bulky lasers, but conceptually independent of the way radiative outcoupling is implemented. With the introduction of a purposely designed small parasitic scattering moment, they can then allow for controllable emission and for independent adjustment of the resonant state and its coherent radiation output, in turn sustaining significantly high Q factors, even when the system size becomes sub-wavelength.

In this work we provide an explicit design and experimental evidence of dark mode lasing using a dielectric-based metasurface. In our case, an explicit dark surface state with gain is outcoupled by an additional scattering mechanism and, therefore, the term "metasurface" refers to the outcoupling implementation alone, although the whole configuration can be considered as one composite metasurface. For low pump we observe luminescence that is characteristic to the dark mode dispersion. For strong pump the unmodified system (i.e., system without scatterer) lases in the dark mode, with the size of the system having direct consequences on the observable far-field: for a theoretically infinite sample, lasing takes place without optical emission, while for a finite-size system lasing is identified in the far-field via the leakage from the edges of the system. By introducing a small, non-resonant scatterer, we demonstrate how we are able to perturb the nonradiating character of the dark mode, thereby turning it (weakly) bright with controllable radiation damping. This allows large-aperture beam-forming emission, that is, emission with controllable k-content (the resolution being reciprocal to the lasing aperture dimensions). The transition from dark to bright mode lasing causes the emission to overtake leakage from the edges of the metasurface, and is observable in the far-field with distinct signatures, in agreement with the theoretical predictions. Our results demonstrate how, by using a specifically tailored scattering mechanism provided by a dedicated metasurface, the radiation damping can be controlled independently from the lasing state. This allows to overcome the rigid coupling between radiative emission, resonant mode, and shape of the metallic nanoparticles in traditional localized plasmon-based nanolasers and is the main point of this paper. We point out, that to facilitate easier fabrication of our laser design, the particular chosen experimental implementation of the dark mode as dielectric waveguide and the use of, essentially, subwavelength electrical gratings for mode quantization and realization of an effective electric current-sheet coupling metasurface bare certain structural similarities to distributed feedback (DFB) lasers.[25–31] These similarities are, however, technical and not conceptual. While in a DFB laser the band structure arising from feedback from distributed multiple scattering is the defining characteristic, in our approach the nature of the dark surface state is generic and can be implemented in various ways not reliant on distributed feedback, including local resonators like meta-atoms. The key point of our approach is that both dark surface-state

and coupling metasurface can be implemented independently. Further analysis of similarities and differences between these concepts can be found below, in the Section 5 of this paper.

## 2. Design, Fabrication, and Experimental Setup

Here, we focus on design parameters for lasing in the near-infrared, in particular, at an emission wavelength of about 880 nm (≈340 THz) (see **Figure 1**). To implement the dark mode, we use an electromagnetically thin homogeneous dielectric slab, realized experimentally as a uniform 40 nm thick TiO_2 film which has refractive index $n = 2.34$ (provided by our ellipsometry measurements). The thin slab supports a TE guided mode (components (H_x, H_y, E_z)) with continuous dispersion that, from the perspective of the outside fields effectively constitutes a TE surface mode. Next, we introduce metallic "grating" wires parallel to the z-direction (which are theoretically infinitely long) and repeat them with a lattice constant $a = 560$ nm periodically along the x-direction, in order to spatially quantize the continuous dark guided mode and achieve a spectrally discrete set of resonant dark surface states. The metal chosen is gold (Au) with thickness 30 nm and width 80 nm and to bond it with the TiO_2 slab we introduce a 10 nm thin Al_2O_3 layer (with refractive index $n = 1.56$), as shown in the inset of Figure 1. Due to the periodic scattering introduced by the metallic grating, a photonic band structure $\omega(k_\parallel)$ emerges with (in-surface) wave vectors k_x that are residue classes modulo $2\pi/a$, splitting the TE surface mode at the edge of the Brillouin zone, $k_x = \pm\pi/a$, into two branches; the higher energy mode at the Brillouin zone edge has antinodes, the lower energy mode
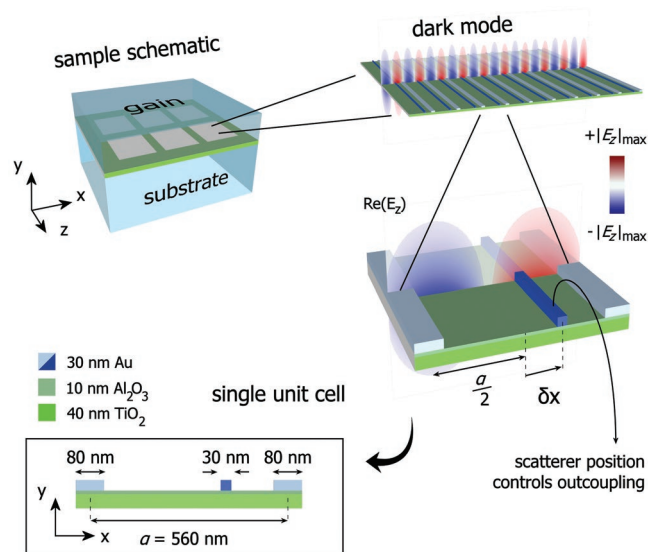
Figure 1. Schematic illustration of the dark mode metasurface laser. Perspective view of sample, metasurface and unit cell, illustrating the spatial distribution of the dark mode. The metasurface consists of N unit cells periodically repeated along the x-direction with periodicity a. A scatterer is used to controllably outcouple the power stored in the dark mode. Inset: Design parameters for operation at 880 nm, illustrated at a cross-section of the unit cell on the x–y-plane. In our design the scatterer is metallic to facilitate the fabrication.

has nodes of the electric field at the spatial positions of the metallic grating wires (see Supporting Information for details). The former of the modes radiates strongly (bright mode), while the latter (illustrated in Figure 1) has no residual moments and is, consequently, dark (note the symmetry in the spatial distribution shown in Figure 1). To explicitly introduce and control the outcoupling of radiated power from the dark mode, we further introduce a weak scatterer in the unit cell, implemented by a second, intercalated grid of wires that are infinite along the z-axis and periodic in x-direction with the same lattice constant a. The outcoupling strength can then be controlled continuously from zero by the displacement, δx, of the scatterer from the center of the unit cell. We choose the scatterer to be also made of gold, having the same thickness as the metallic grating wires (30 nm) but a smaller width of only 30 nm, in order to perturb the dark mode only slightly. The strong near-fields of the bound dark state that extends outside and projects from the dielectric slab's surface enable sufficient coupling of the dark mode with the gain medium, which we place as an external thin liquid layer on top of the slab. The whole system is supported by a BK7 glass substrate of refractive index $n = 1.5214$ and the gain medium (IR-792 solution) is index-matched with the substrate using a solvent mixture of ethylene glycol (ethane-1,2-diol) (EG) and benzyl alcohol (BA) mixed in a 1:1 volume ratio (IR-792 is added to the EG:BA solution in 25 mM concentration). The gain medium emits around ≈850 nm, and is chosen in order to promote lasing into the dark mode. For our numerical simulations we perform full-wave vectorial finite element method (FEM) simulations with the commercial software COMSOL Multiphysics, using Johnson and Christy data[32] for the Au permittivity. A scanning electron microscopy (SEM) image of the fabricated sample viewed from the top is shown in **Figure 2**a. The broad white lines are wires of the quantizing grating, the thinner white lines that are slightly offset from the center of the unit cell are the weak scatterers. In order to experimentally obtain the band structure of the dark mode and compare with the numerical simulations, angle and wavelength resolved transmission measurements were performed using a halogen lamp as a white light source illuminating the sample from the other side. For the lasing measurements, the sample was pumped with a fs pulsed laser with a pump spot of approximately 100 μm in reflection geometry with an incidence angle of about 45°. The emitted luminescence and lasing radiation of the sample was collected, angle and wavelength resolved around the direction normal to the surface and analyzed, depending on pump laser power. The experimental measurement setup is illustrated schematically in Figure 2c. It combines two optical paths: an ultrafast NIR pump laser (780 nm, 1 kHz, 150 fs) is used to excite the dye from the structure side (through the bottom substrate) of the sample. The emitted light from the sample is collected using a 10 × 0.3 NA microscope objective (L2). In order to obtain angle-resolved spectral data, the back focal plane (BFP) of the objective is imaged using lenses L3 and L4 to the entrance slit of an imaging spectrometer. The entrance slit selects $k_z \approx 0$, while the spectrum of light emitted to different angles $\Theta(k_x)$ is obtained as a 2D image, with pixel rows corresponding to different angles and columns to different wavelengths. The second optical path in Figure 2c is
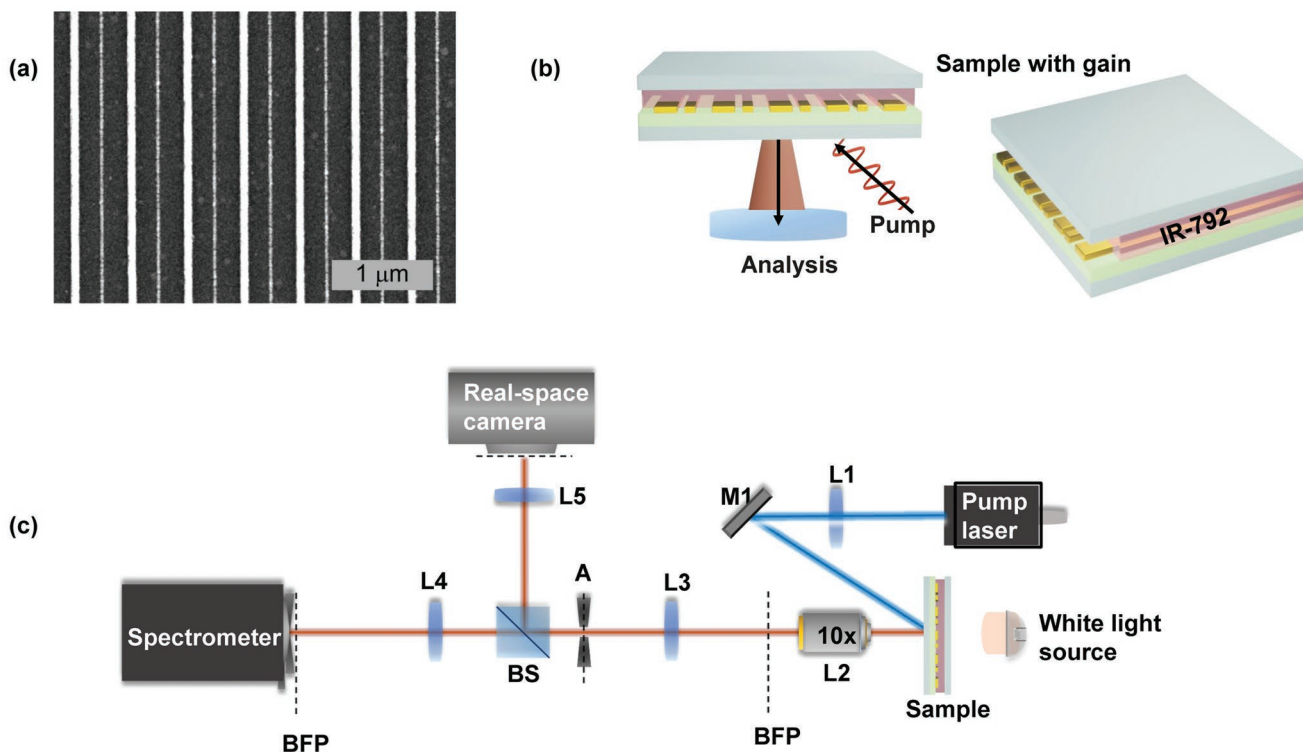
Figure 2. Experimental sample and measurement setup. a) Scanning electron microscopy image of the fabricated sample with $\delta x \approx 20$ nm offset for the scatterer. b) Illustration of the sample with the liquid gain medium. A 0.5 mm silicon spacer and a second BK7 glass substrate is used to create a cavity for the dye solution (pink). Due to the thickness of the gain layer, the optical pumping illuminates the sample from below. c) Measurement setup (see text).

ADVANCED
SCIENCE NEWS
www.advancedsciencenews.com

ADVANCED
OPTICAL
MATERIALS
www.advopticalmat.de

used for transmission measurements and for selecting the measured area. A halogen lamp is used as a white light source, and an adjustable aperture A is placed on the real-space image formed by the objective L2 and lens L3. The beam splitter BS and lens L5 are used to relay a part of the real space image to a camera (FLIR Grasshopper 3GS3-U3-32S4M-C), which is used for navigation and matching the aperture size to the structures. The light passing through the beam splitter and L4 will form the BFP image on the spectrometer input slit as in the emission measurements.
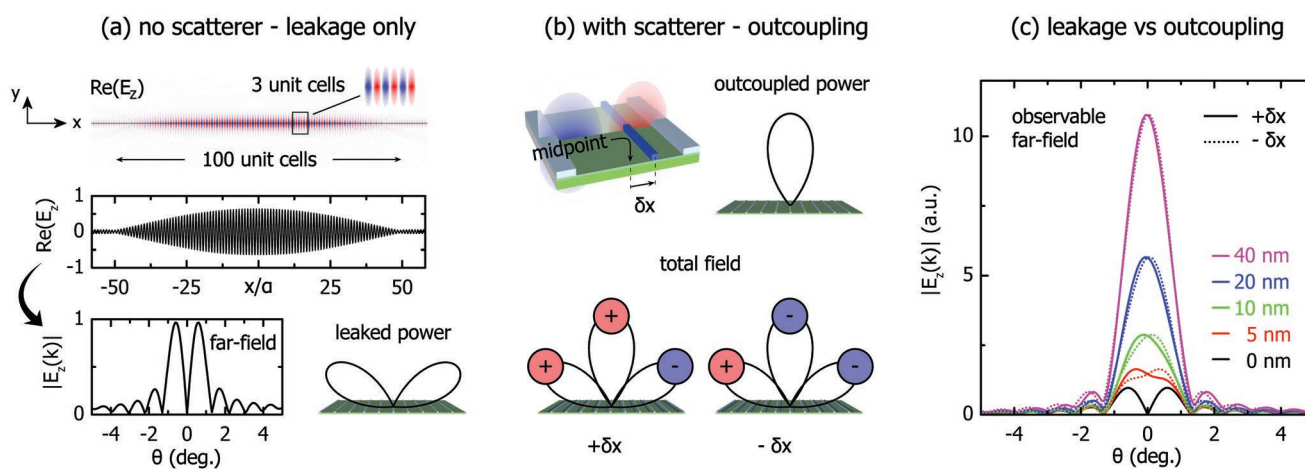
3. Theory of Operation

Above the lasing threshold stimulated emission from the gain subsystem (here a pumped dye) takes place directly into the photons of the dark mode, and the electromagnetic energy remains stored in the dark mode, which serves as the nanolaser resonator, without coupling to a free-space radiating far-field. Ideally, for a metasurface of theoretically infinite extent, the radiation channel is completely closed and, therefore, no far-field should be observable. This means that, to identify whether the absence of radiation implies dark mode lasing or no lasing at all, near-field measurements would be required. In practice, however, the finite extent of the metasurface introduces leakage from the edges of the system, which can be exploited to differentiate between the two cases. This is shown in **Figure 3**a for a system of 100 unit cells. Due to the finite size of the metasurface, the extended bound state is a standing wave formed by the superposition of the $+k$, $-k$ bound propagating modes that are reflected at the edges of the finite sample, acquiring a sine-like standing wave envelope, as shown in $Re(E_z)$. This leads to the occurrence of weak but nonzero radiating moments that become stronger closer to the edges. As a result, the leaked power leads to a characteristic double-lobe radiation pattern in the far-field. The introduction of a weak scatterer has the effect of turning the dark mode partially bright with strong radiating moments contributing coherently from each unit cell along the surface. This is expected to be detectable in the far-field as a single-lobe radiation pattern at $k_x = 0$, as shown schematically in Figure 3b, top. The outcoupling strength can be tuned via the scatterer position and, hence, the amplitude of the radiation lobe can be fully controlled via the displacement of the scatterer from the center of the unit cell, δx. Clearly, while the leakage is always present, the outcoupling can be tuned to be either absent ($\delta x = 0$) or present ($\delta x \neq 0$) with tunable strength. Additionally, depending on the direction of the scatterer displacement (the sign of δx), the phase of the main lobe can be phase-shifted by π, as shown schematically in Figure 3b, bottom. Therefore, the interplay between the two contributions can lead to different radiation patterns, ranging from double-lobe (no outcoupling, $\delta x = 0$), to single asymmetric lobe (weak outcoupling, $\delta x = 5...20$ nm), and to single symmetric lobe (strong outcoupling, $\delta x = 40$ nm), as shown in the calculations of Figure 3c. Also shown in the same panel is the calculated far-field for negative δx (scatterer displacement toward the opposite direction). To summarize, the results show the gradual transition from the symmetric double-lobe pattern to a single asymmetric lobe with increasing outcoupling strength, the asymmetry being dependent on the sign of δx.

4. Results

The presence of the dark mode manifests in various ways. Radiative emission originating from the lasing dark mode, as discussed in the previous section, is expected to be identifiable in the far-field as a double-lobe pattern angular distribution, which turns into a single-lobe pattern as the increasing
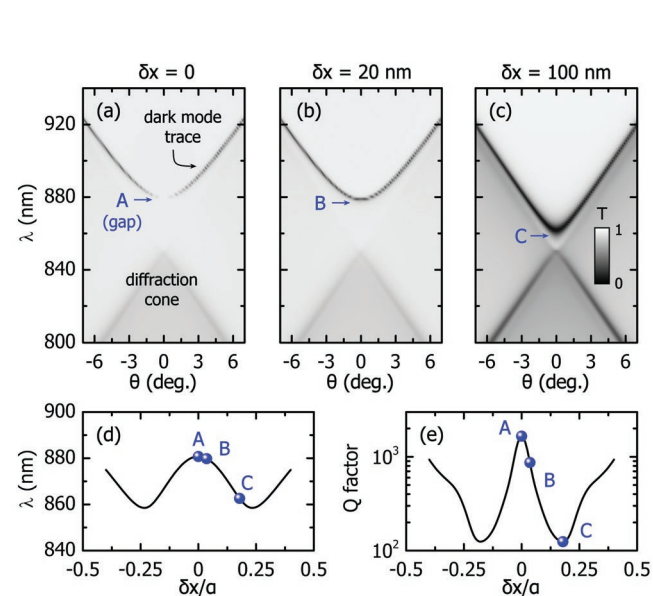

Figure 3. Theory of operation. a) In the abscence of the scatterer, undesired leakage occurs from the edges of the metasurface, as can be seen in the spatial distribution of $Re(E_z)$ at the vicinity of the metasurface (top panel); a cross-section of $Re(E_z)$ at $y = 0$ is shown in the middle panel. In the far-field, leakage forms a double-lobe radiation pattern (bottom panel). b) With the scatterer, the intented outcoupling is expected to form a single-lobe radiation pattern in the forward direction. However, due to undesired leakage, the total field is a weighted superposition of both contributions, leading to asymmmetric radiation patterns; the shape depends on the relative strength between leakage and outcoupling, that is on the magnitude of the scatterer displacement δx, and the asymmetry depends on the sign of δx. c) Far-field angular distribution in the presence of scatterer as a function of the outcoupling strength, which is controlled by δx. With increasing δx outcoupling dominates leakage and the two far-field lobes merge into a single asymmetric lobe.

intended outcoupling starts to dominate over leakage with increasing δx. Additionally, the band structure of the modes can be probed with transmission measurements in the system without gain. In this case the gain medium simply is a typical dielectric without providing amplification. Next we present linear scattering calculations, which show how the dark mode is expected to manifest its presence in transmittance spectra. We also present the corresponding experimental transmission measurements, which verify that the fabricated metasurface indeed supports the theoretically expected dark mode.

4.1. Linear Scattering

In the simulations, in order to probe the mode structure for the system without gain, we first apply a z-polarized wave across the range $800 - 1000$ nm (TE polarization), normally incident to the metasurface. With the scatterer placed in the middle of the unit cell ($\delta x = 0$) the mode is completely dark and, hence, the incident wave cannot couple and shows no spectral feature in transmission. However, with keeping the E-field polarization parallel to the metallic wires and scanning the incident angle θ on the $x - y$ plane, we are departing from the Brillouin zone edge. In turn now the incident wave couples to the dark mode (which is completely dark only for $k_x = 0$), inducing a dip in the transmittance that marks the dark mode frequency and disappears exactly at $k_x = 0$, as shown in the parabolic trace of **Figure 4**a. The parabolic dispersion of the dark mode is clearly traced by the transmittance dip, as we also verify with separate eigenmode simulations (see Supporting Information).

With $\delta x = 20$ nm the onset of outcoupling allows for coupling of the incident wave with the dark mode at normal incidence, which is seen in Figure 4b as closing the gap at the parabola apex. With further increase of outcoupling ($\delta x = 100$ nm, Figure 4c) the gap remains closed and the parabola shifts to shorter wavelengths. The trace of the parabola apex as a function of $\delta x/a$ is shown in Figure 4d and is characteristic to the dark mode. On the other hand, the trace of the transmittance dip residing at shorter wavelengths ($\lambda < 850$ nm) remains immobile with increasing outcoupling and has a linear, rather than a parabolic, shape; this marks the first diffraction order, the apex of which depends only on the periodicity a, which does not change (see Supporting Information).

Another verifiable feature of dark mode operation is the characteristic Q factor variation with shifting the position of the scatterer,[21–23] as shown in Figure 4e. For $\delta x = 0$ (middle of the unit cell), the Q factor acquires its maximum value $Q = 1865$, which is limited only by the dissipative losses of the metal. With increasing δx, the coupling strength changes according to the shape of the dark mode; at positions where the fields are higher, the coupling is stronger and, hence, the radiation damping is stronger and the Q factor smaller. This is reflected in the non-monotonic change observed in Figure 4e, as retrieved from eigenmode simulations at the parabola apex. The lasing threshold changes inversely with the Q factor, and, as a direct consequence, its lowest value is expected for $\delta x = 0$.

To verify the theoretically expected behavior, in the experiments we first perform transmittance measurements, which are shown in **Figure 5**a–c corresponding to the three cases
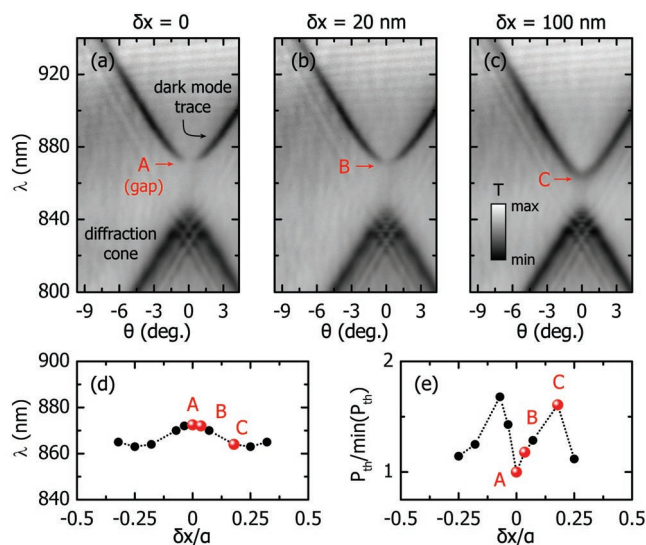
Figure 4. Linear scattering simulations as a function of the scatterer position. a–c) Transmittance spectra under TE incident waves as a function of the incidence angle θ for no outcoupling (a), weak outcoupling (b), and strong outcoupling (c). d) Trace of the parabola apex shown in (a)–(c), marking the dark mode operation point. The trace agrees with the dark mode wavelength retrieved separately from eigenmode simulations. e) Q factor calculated from eigenmode simulations. The points denoted with A, B, and C mark the operation points indicated in (a)–(c).

Figure 5. Linear scattering experiments as a function of the scatterer position. a–c) Transmittance spectra under TE incident waves as a function of the incidence angle θ for no outcoupling (a), weak outcoupling (b), and strong outcoupling (c). d) Trace of the parabola apex shown in (a)–(c), in qualitative agreement with the theoretically expected behavior shown in Figure 4(d). e) Lasing threshold (normalized to the minimum threshold) showing the expected inverse change with the calculated Q factor shown in Figure 4(e). The points denoted with A, B, and C mark the operation points indicated in the three panels of (a)–(c) and the dotted lines connect the experimental data points.

examined theoretically in Figure 4a–c, respectively. Clearly, in the experiment we observe a gap at the parabola apex for $\delta x = 0$, which disappears with increasing scatterer displacement. Additionally, the parabola apex moves to shorter wavelengths and the diffraction cone remains immobile, as predicted by the simulations. In Figure 5d the position of the parabola apex is presented as a function of $\delta x/a$, showing the qualitatively expected behavior. Next, we record the pump power required for the system to start lasing. In Figure 5e we plot the lasing threshold as a function of $\delta x/a$, normalized to its lowest value, which is observed for $\delta x = 0$ as theoretically predicted. By varying the scatterer position we also observe the expected characteristic inverse dependence of the lasing threshold with the Q factor shown in Figure 4e. The observed slight asymmetry for $\pm \delta x/a$ can be attributed possibly to fabrication irregularities and the onset of lasing in other modes, especially when the outcoupling is strong and the dark mode Q factor is suppressed. Importantly, the experimental measurements show the theoretically expected qualitative trend in all key points that mark dark mode operation, namely: a) the existence of a gap at the parabola apex ($k_x = 0$) for no outcoupling and its disappearance with outcoupling; b) the characteristic non-monotonic change of the λ of the parabola apex with variable outcoupling; and c) the characteristic non-monotonic change of the Q factor and the inverse behavior of the lasing threshold, the latter acquiring its minimum value for $\delta x = 0$.

4.2. From Luminescence to Lasing

In this section we present experimental measurements of the light emitted from the metasurface under optical pumping. In **Figure 6** we use two samples, one with no scatterer (Figure 6a,c) and one with the scatterer placed in the middle of the unit cell (Figure 6b,d).

For low pump, both systems reside below the lasing threshold and we observe luminescence. The presence of all k-modes in the incoherent luminescence effectively traces the parabolic dispersion of the dark mode (Figure 6a,b). This is a direct consequence of the high density of optical states provided by the dark mode with respect to the continuum and is a means for independently identifying the presence of the dark mode. In the absence of scatterer (Figure 6a) we observe the suppression of luminescence at the parabola apex, which is a clear indication that the mode is dark. With the scatterer present (Figure 6b) luminescence is restored at the parabola apex, which is a direct consequence of the fact that the mode is slightly bright. Note that, the observed radiative coupling occurs despite the scatterer residing in the middle of the unit cell. This is possibly due to irregularities in the cross-section of the scatterer, as also seen in Figure 2, leading to weak outcoupling. In both examples, the wide bright region around 850 nm marks the emission from the bulk gain material.

For high pump, both systems pass on to dark-state lasing. In Figure 6c, where the mode is completely dark and leakage dominates, dark-state lasing is identified in the theoretically expected double-lobe radiation pattern observed at the parabola apex. The same plot is overlapped with a copy of itself in saturated
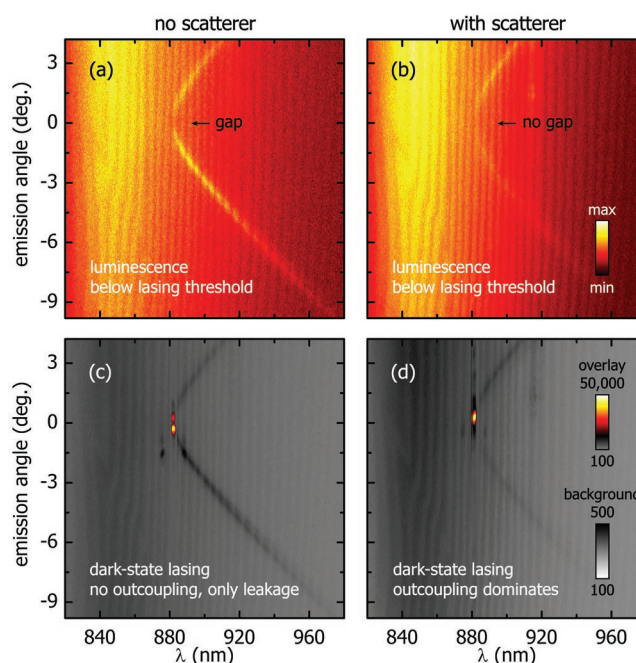

Figure 6. Dark versus bright lasing. a,c) No scatterer, and b,d) scatterer placed at $\delta x \approx 0$. For low pump (a,b) the luminescence footprint marks the dark mode parabolic dispersion, indicating that the pump power is channeled into the dark mode. For strong pump (c,d) the excited states collapse into a single lasing dark mode; without the scatterer, for an infinite system the lasing mode should be completely dark, however due to leakage from the edges of the finite-size metasurface, dark mode lasing can be identified in the far-field as a double lobe pattern. With the scatterer present, the dark mode is controllably turned into bright, and lasing into the dark mode is identified in the far-field as a single lobe pattern due to intentional outcoupling. The gain emission wavelength is at 850 nm, and can be identified in the wide bright region in (a) and (b). To mitigate the contrast between the luminescence background and the lasing peak we plot the region around the lasing wavelength (880 ± 2 nm) at a different scale than the background.

grayscale, to clarify that the double-lobe pattern resides at the apex of the parabola, that is, it is indeed the dark mode that is lasing. In Figure 6d, where the mode is weakly bright, outcoupling dominates leakage and dark-state lasing is identified in the theoretically expected single-lobe pattern observed at the parabola apex.

Last, in **Figure 7** we examine the case of stronger outcoupling, that is with $\delta x = \pm 20$ nm. The sign change in δx corresponds to purely symmetric metasurfaces and the observed lasing behavior should, therefore, not change. The dashed lines that mark the single-lobe lasing peak for each case, indeed verify that the position of the lasing peak does not depend on the scatterer position side.

Using a nonlinear color scale amplifying low values in Figure 6c,d and Figure 7 lets us simultaneously visualize the lasing peaks together with the weak residual luminescence parabola at the same pump level. This allows to demonstrate the relative position of lasing peaks versus dark mode dispersion even in the case of pump induced index change of the gain medium.
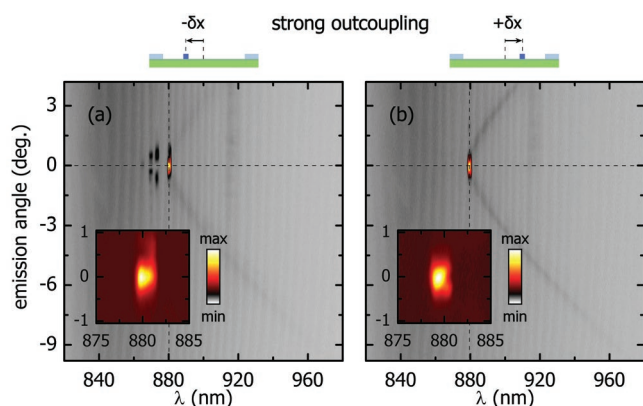
Figure 7. Bright lasing with strong outcoupling. The scatterer is placed symmetrically with respect to the center of the unit cell with displacement $\delta x = -20$ nm in (a) and $\delta x = +20$ nm in (b). In (a) the multiple peaks located at slightly shorter wavelengths from the parabola apex have intensities ≈2 orders of magnitude lower than the dark-state lasing peak and are further suppressed for higher pump; here the measurements are taken slightly above the lasing threshold. The inset shows a magnification around 880 nm and 0°, where the characteristic single-lobed lasing peak is clearly seen.

5. Discussion

With the conceptual separation of the implementation of the lasing state from radiative coupling, a key feature that is missing from the numerous contemporary nanolaser approaches, we aim to provide a new perspective for future designs by practically bringing together the established nanolasing techniques with the well-studied functionalities of metasurfaces. What we demonstrate is that controllable radiative emission, which is the main advantage of our metasurface laser compared to existing nanolaser approaches, is possible with three ingredients: a) a resonant dark surface state; b) a gain medium coupled with and lasing into this dark mode; and c) a weakly coupled radiative metasurface that (ideally) only slightly perturbs the resonant/lasing dark surface state and has the only purpose of introducing controllable, but relatively weak, coupling between the near-field of the dark state and propagating vacuum modes. In our experiments, to simplify the fabrication, we chose to implement the dark mode on a dielectric thin film as a bound standing wave guided mode and we used metallic wires to pin the E-field and achieve discrete sets of resonant modes. Alternatively, we could have used typical plasmonic components, such as split-ring-resonators,[33] cut wire pairs,[34] or metallic nanodisks[24] to implement the dark surface state; that is the concept applies equally well to both fully dielectric[35] or plasmonic lasers.[36] Note that, our system is not plasmonic per se, that is lasing does not take place into a plasmonic mode; the metasurface does involve metallic parts as a means for quantizing the dark state, however the field has nodes on the metal grating and is concentrated in the dielectric film in between the metallic wires. Additionally, both grating and scatterers could be made from dielectrics with high enough index contrast, making the metasurface completely dielectric. This helps to reduce dissipative losses to a minimum, which is particularly relevant for the nonresonant outcoupling scatterers, because they are exposed to finite field, as opposed to the field nodes at the grating wires. As a compromise between performance and fabricability in our samples we

chose to fabricate both grating and outcoupling scatterers from a single metalization layer. We would also like to point out that certain structural elements in our demonstrated system, such as the use of a periodic subwavelength grating structure, the spatially antisymmetric guided standing wave and the emission that occurs perpendicularly to the surface, bare similarities to popular DFB lasers.[25–31] However, it is important to clarify that our approach is more general and goes beyond the distributed feedback aspect of the specific implementation. In DFBs the conceptually primary concern is to provide feedback to guided modes by (distributed) coherent multiple scattering along the surface, to form a surface mode band structure with a bandgap that leads to localization of the mode in the surface with dark and bright "surface" states, associated with the corresponding multiple-scattering-induced bandgap in the surface mode dispersion; the outcoupling is consequential. In our approach, the conceptually primary concern is the separation of lasing and outcoupling and, therefore, our approach is –in principle– agnostic of the particular implementation of the dark surface state; the concept is quite general and goes beyond the specific configuration demonstrated here. For example, a single unit cell inside a waveguide with hard boundary conditions eliminates the "distributed" feedback in favor of a simple cavity for dark state (perpendicular to the length of the waveguide) and conceptually achieves controllable radiation damping and out-coupling (see for example the configuration in ref. [37]). Or, the same concept can be achieved with any localized resonators that implement the dark local resonance by mutually cancelling their radiating dipole moments by clever geometric arrangement, for example conjugated split-ring-resonators,[33] EIT configurations,[38] or non-radiative anapole-type meta-atoms.[39,40] Regardless of the particular implementation, it is necessary to have a controllable out-coupling mechanism, that is a coupling metasurface, which we here implemented as a rather trivial sub-wavelength grating, which generates homogeneous effective electric surface currents that radiate plane waves normal to the surface. The term "metasurface" signifies the universality of the out-coupling mechanism as a radiating effective electromagnetic current sheet and its conceptual independence on the implementation of the dark lasing state. Additionally, it emphasizes the beam-forming capabilities enabled by more sophisticated possible subwavelength gratings (metasurfaces) that are spatially modulated and/or can implement simultaneously both electric and magnetic effective sheet currents that enable, for example, one-sided emission,[21,22] off-normal emission,[23] emission into focus, and formation of structured beams (vortex beams, Bessel beams, and so on), all without lenses; these are functionalities that bring a distinctive interest in metasurface lasers. In contrast to traditional nanolasers, where the goal is to concentrate lasing into small volumes, the extended nature of surface states enables large aperture lasers, and the metasurface offers the desired spatial control of the emitted light for achieving unique beam properties without the use of external optical components. Because of the notion of the surface state and metasurface, the concept can be realized all in a 2D geometry. Importantly, due to the flexibility to enable or suppress radiative coupling, the operation of the metasurface laser is not limited to coupling into propagating radiation; it can be used to directly couple the lasing surface state to other surface bound waves, for examle, plasmons in graphene or other 2D systems,

**ADVANCED
SCIENCE NEWS**

www.advancedsciencenews.com

**ADVANCED
OPTICAL
MATERIALS**

www.advopticalmat.de

essentially replacing far-field approaches (oblique incidence or periodic patterning, for matching the high local k's), with direct, controllable, near-field excitation.

6. Conclusion

In this work we fabricated and experimentally demonstrated dark-state lasing with controllable radiation damping in a metasurface laser design made using a dark bound state in a thin, low-loss dielectric film in combination with a tightly coupled, weakly radiative metasurface metasurface. We demonstrated how, with the aid of small -nonresonant- scatterers, the dark mode can be made partially bright, allowing for power outcoupling in a controllable manner without significantly disturbing the resonant dark lasing state. This validates the design concept of separating the gain-coupled resonant photonic state responsible for macroscopic stimulated emission from the coupling to a specific free-space propagating field optical output. We identified the dark mode operation with distinct, experimentally observable signatures under linear scattering measurements (no pump) and luminescence/lasing (with pump), verifying that the experimental measurements agree with the theoretically expected behavior. The experimental results are supported by and in good agreement with detailed numerical simulations of the lasing setup. The scalability of our design, here implemented for lasing in the near-infrared, enables ultrathin coherent light sources with controllable emission from the infrared to the visible. Due to its planar geometry, our design is also ideal for layer-by-layer fabrication, offering a feature that is crucial for future large scale on-chip integrated nanolasers designed for free-space beam-forming emission.

Supporting Information

Supporting Information is available from the Wiley Online Library or from the author.

Conflict of Interest

The authors declare no conflict of interest.

Data Availability Statement

The data that support the findings of this study are available from the corresponding author upon reasonable request.

[1] A. E. Siegman, *Lasers*, University Science Books, Sausalito, CA **1986**.
[2] D. J. Bergman, M. I. Stockman, *Phys. Rev. Lett.* **2003**, *90*, 027402.
[3] M. I. Stockman, *Nat. Photonics* **2008**, *2*, 327.
[4] N. I. Zheludev, S. L. Prosvirnin, N. Papasimakis, V. A. Fedotov, *Nat. Photonics* **2008**, *2*, 351.
[5] R. F. Oulton, V. J. Sorger, T. Zentgraf, R.-M. Ma, C. Gladden, L. Dai, G. Bartal, X. Zhang, *Nature* **2009**, *461*, 629.
[6] M. A. Noginov, G. Zhu, A. M. Belgrave, R. Bakker, V. M. Shalaev, E. E. Narimanov, S. Stout, E. Herz, T. Suteewong, U. Wiesner, *Nature* **2009**, *460*, 1110.
[7] P. Berini, I. De Leon, *Nat. Photonics* **2012**, *6*, 16.
[8] S. Wuestner, A. Pusch, K. L. Tsakmakidis, J. M. Hamm, O. Hess, *Phys. Rev. Lett.* **2010**, *105*, 127401.
[9] O. Hess, J. B. Pendry, S. A. Maier, R. F. Oulton, J. M. Hamm, K. L. Tsakmakidis, *Nat. Mater.* **2012**, *11*, 573.
[10] J. M. Taskinen, A. J. Moilanen, H. Rekola, K. Kuntze, A. Priimagi, P. Törmä, T. K. Hakala, *ACS Photonics* **2020**, *7*, 2850.
[11] V. Mylnikov, S. T. Ha, Z. Pan, V. Valuckas, R. Paniagua-Domínguez, H. V. Demir, A. I. Kuznetsov, *ACS Nano* **2020**, *14*, 7338.
[12] E. Tiguntseva, K. Koshelev, A. Furasova, P. Tonkaev, V. Mikhailovskii, E. V. Ushakova, D. G. Baranov, T. Shegai, A. A. Zakhidov, Y. Kivshar, S. V. Makarov, *ACS Nano* **2020**, *14*, 8149.
[13] A. Tripathi, H.-R. Kim, P. Tonkaev, S.-J. Lee, S. V. Makarov, S. S. Kruk, M. V. Rybin, H.-G. Park, Y. Kivshar, *Nano Lett.* **2021**, *21*, 6563.
[14] A. Kodigala, T. Lepetit, Q. Gu, B. Bahari, Y. Fainman, B. Kanté, *Nature* **2017**, *541*, 196.
[15] S. T. Ha, Y. H. Fu, N. K. Emani, Z. Pan, R. M. Bakker, R. Paniagua-Domínguez, A. I. Kuznetsov, *Nat. Nanotechnol.* **2018**, *13*, 1042.
[16] M. Wu, S. T. Ha, S. Shendre, E. G. Durmusoglu, W.-K. Koh, D. R. Abujetas, J. A. Sánchez-Gil, R. Paniagua-Domínguez, H. V. Demir, A. I. Kuznetsov, *Nano Lett.* **2020**, *20*, 6005.
[17] M.-S. Hwang, H.-C. Lee, K.-H. Kim, K.-Y. Jeong, S.-H. Kwon, K. Koshelev, Y. Kivshar, H.-G. Park, *Nat. Commun.* **2021**, *12*, 4135.
[18] D. Smirnova, A. Tripathi, S. Kruk, M.-S. Hwang, H.-R. Kim, H.-G. Park, Y. Kivshar, *Light: Sci. Appl.* **2020**, *9*, 127.
[19] Z.-Q. Yang, Z.-K. Shao, H.-Z. Chen, X.-R. Mao, R.-M. Ma, *Phys. Rev. Lett.* **2020**, *125*, 013903.
[20] Z.-K. Shao, H.-Z. Chen, S. Wang, X.-R. Mao, Z.-Q. Yang, S.-L. Wang, X.-X. Wang, X. Hu, R.-M. Ma, *Nat. Nanotechnol.* **2020**, *15*, 67.
[21] S. Droulias, A. Jain, T. Koschny, C. M. Soukoulis, *Phys. Rev. Lett.* **2017**, *118*, 073901.
[22] S. Droulias, A. Jain, T. Koschny, C. M. Soukoulis, *Phys. Rev. B* **2017**, *96*, 155143.
[23] S. Droulias, T. Koschny, C. M. Soukoulis, *ACS Photonics* **2018**, *5*, 3788.
[24] T. K. Hakala, H. T. Rekola, A. I. Väkeväinen, J.-P. Martikainen, M. Nečada, A. J. Moilanen, P. Törmä, *Nat. Commun.* **2017**, *8*, 13687.
[25] H. Kogelnik, C. V. Shank, *Appl. Phys. Lett.* **1971**, *18*, 152.
[26] H. Kogelnik, C. V. Shank, *J. Appl. Phys.* **1972**, *43*, 2327.
[27] W. Ng, A. Yariv, *Appl. Phys. Lett.* **1977**, *31*, 613.
[28] R. Kazarinov, C. Henry, *IEEE J. Quantum Electron.* **1985**, *21*, 144.
[29] M. Kasraian, D. Botez, *Appl. Phys. Lett.* **1995**, *67*, 2783.

**ADVANCED
SCIENCE NEWS**

www.advancedsciencenews.com

**ADVANCED
OPTICAL
MATERIALS**

www.advopticalmat.de

[30] L. Mahler, A. Tredicucci, F. Beltram, C. Walther, J. Faist, H. E. Beere, D. A. Ritchie, *Appl. Phys. Lett.* **2010**, *96*, 191109.

[31] Y. Jin, L. Gao, J. Chen, C. Wu, J. L. Reno, S. Kumar, *Nat. Commun.* **2018**, *9*, 1407.

[32] P. B. Johnson, R. W. Christy, *Phys. Rev. B* **1972**, *6*, 4370.

[33] M. Fang, N.-H. Shen, W. E. I. Sha, Z. Huang, T. Koschny, C. M. Soukoulis, *Phys. Rev. Lett.* **2019**, *122*, 027401.

[34] G. Dolling, C. Enkrich, M. Wegener, J. F. Zhou, C. M. Soukoulis, S. Linden, *Opt. Lett.* **2005**, *30*, 3198.

[35] M.-S. Hwang, H.-R. Kim, K.-Y. Jeong, H.-G. Park, Y. Kivshar, *Nanophotonics* **2021**, *10*, 3599.

[36] S. I. Azzam, A. V. Kildishev, R.-M. Ma, C.-Z. Ning, R. Oulton, V. M. Shalaev, M. I. Stockman, J.-L. Xu, X. Zhang, *Light: Sci. Appl.* **2020**, *9*, 90.

[37] A. Jain, P. Tassin, T. Koschny, C. M. Soukoulis, *Phys. Rev. Lett.* **2014**, *112*, 117403.

[38] Y. Yang, I. I. Kravchenko, D. P. Briggs, J. Valentine, *Nat. Commun.* **2014**, *5*, 5753.

[39] V. Savinov, N. Papasimakis, D. P. Tsai, N. I. Zheludev, *Commun. Phys.* **2019**, *2*, 69.

[40] E. Takou, A. C. Tasolamprou, O. Tsilipakos, E. N. Economou, *Phys. Rev. B* **2019**, *100*, 085431.